nature nanotechnology

ARTICLES

https://doi.org/10.1038/s41565-018-0141-z

Carbon nanotube bundles with tensile strength over 80 GPa

Yunxiang Bai[1,2,5], Rufan Zhang[1,5*], Xuan Ye[2,3,5], Zhenxing Zhu[1,2], Huanhuan Xie[1,2], Boyuan Shen[1], Dali Cai[1], Bofei Liu[4], Chenxi Zhang[1,2], Zhao Jia[1], Shenli Zhang[1], Xide Li[2,3*] and Fei Wei[1,2*]

Carbon nanotubes (CNTs) are one of the strongest known materials. When assembled into fibres, however, their strength becomes impaired by defects, impurities, random orientations and discontinuous lengths. Fabricating CNT fibres with strength reaching that of a single CNT has been an enduring challenge. Here, we demonstrate the fabrication of CNT bundles (CNTBs) that are centimetres long with tensile strength over 80 GPa using ultralong defect-free CNTs. The tensile strength of CNTBs is controlled by the Daniels effect owing to the non-uniformity of the initial strains in the components. We propose a synchronous tightening and relaxing strategy to release these non-uniform initial strains. The fabricated CNTBs, consisting of a large number of components with parallel alignment, defect-free structures, continuous lengths and uniform initial strains, exhibit a tensile strength of 80 GPa (corresponding to an engineering tensile strength of 43 GPa), which is far higher than that of any other strong fibre.

Superstrong fibres are in great demand in many high-end fields such as sports equipment, ballistic armour, aeronautics, astronautics and even space elevators[1]. In 2005, the US National Aeronautics and Space Administration (NASA) launched a 'Strong Tether Challenge', aiming to find a tether with a specific strength up to 7.5 GPa cm^3 g^{-1} for the dream of making space elevators[2]. Unfortunately, there is still no winner for this challenge. The specific strength of existing fibres such as steel wire ropes (about 0.05–0.33 GPa cm^3 g^{-1})[3], carbon fibres (about 0.5–3.5 GPa cm^3 g^{-1})[4] and polymer fibres (about 0.28–4.14 GPa cm^3 g^{-1})[3] is far lower than 7.5 GPa cm^3 g^{-1}). Carbon nanotubes, with inherent tensile strength higher than 100 GPa and Young's modulus over 1 TPa (refs. [5–7]), are considered one of the strongest known materials[8]. Generally, there are three types of CNT: agglomerated CNTs[9], vertically aligned CNT (VACNT) arrays[10,11] and ultralong horizontally aligned CNT (HACNT) arrays ('ultralong CNTs' for short)[12,13]. Almost all the reported CNT fibres are fabricated using agglomerated CNTs or VACNT arrays with lengths less than a few hundred micrometres and with plenty of structural defects and impurities, giving those CNT fibres a tensile strength ranging from about 0.5 to 8.8 GPa (refs.[14–17]), which is much lower than that of single CNTs. The main reason is that the short CNT components in these fibres entangle or overlap with each other, primarily because of van der Waals interactions, which does not make full use of the inherent strength of single CNTs. In comparison, ultralong CNTs should have great advantages in fabricating fibres because of their macroscale lengths (ranging from centimetres to decimetres)[18], neat surface, perfect structures and super-parallel alignments[8]. But because the production of ultralong CNTs is extremely low[1], there have been no reports of fibres fabricated using ultralong CNTs, so the question of whether ultralong CNTBs possess equivalent strength to single CNTs has remained open. Owing to the difficulties of manipulating single CNTs and of nanoscale force measurement, it also remains ambiguous how the overall strength of CNT fibres is affected by factors such as the component number, length and alignment. It is important to address these issues for the fabrication of ultralong-CNT-based fibres with excellent mechanical properties.

Fabrication of CNT bundles

We have fabricated CNTBs that are several centimetres long, using ultralong CNTs with defined number and parallel alignment, to quantitatively investigate the relationship between the tensile strength of ultralong-CNT-based fibres and their components (Fig. 1a). Generally, the ultralong CNTs are synthesized through a gas-flow-directed chemical vapour deposition (CVD) method with parallel orientations and large intertube distance on flat substrates. The resulting CNTs usually have one to three walls with perfect structures (Fig. 1b)[1,8]. During the growth process, the ultralong CNTs float in the gas flow, which directly guides their orientation[19]. To fabricate ultralong CNTBs, we propose an in situ gas-flow focusing (GFF) strategy to assemble individual CNTs into bundles (Fig. 1c,d and Supplementary Fig. 1). With the GFF effect of the gas barriers, adjacent CNTs gradually assemble togther because of the van der Waals interactions between them, forming ultralong CNTBs with various component numbers (Fig. 1e–i). We previously reported the optical visualization of individual CNTs by decoration with TiO_2 nanoparticles (Fig. 1j–l), which greatly assists in the rapid location and manipulation of individual CNTs under the optical microscope[20]. It has been confirmed that the interaction between the TiO_2 nanoparticles and the CNTs/CNTBs is dominated by van der Waals interactions[21,22], which is much lower than the mechanical strength of CNTs and has no impact on the Raman spectra or the mechanical strength of CNTs/CNTBs (Supplementary Text 1 and 2)[20,23]. The same method is used in this work. Both single CNTs and CNTBs can be clearly observed under the optical microscope (Fig. 1l,m and Supplementary Figs. 2 and 3), scanning electron microscope (SEM, Fig. 1e,f), atomic force microscope (AFM, Fig. 1o) and transmission electron microscope (TEM, Fig. 1g–i,p).

[1]Beijing Key Laboratory of Green Chemical Reaction Engineering and Technology, Department of Chemical Engineering, Tsinghua University, Beijing, China. [2]Center for Nano and Micro Mechanics, Tsinghua University, Beijing, China. [3]Department of Engineering Mechanics, AML, Tsinghua University, Beijing, China. [4]Department of Materials Science and Engineering, Stanford University, Stanford, CA, USA. [5]These authors contributed equally: Yunxiang Bai, Rufan Zhang, Xuan Ye. *e-mail: zhangrufan@tsinghua.edu.cn; lixide@tsinghua.edu.cn; wf-dce@tsinghua.edu.cn

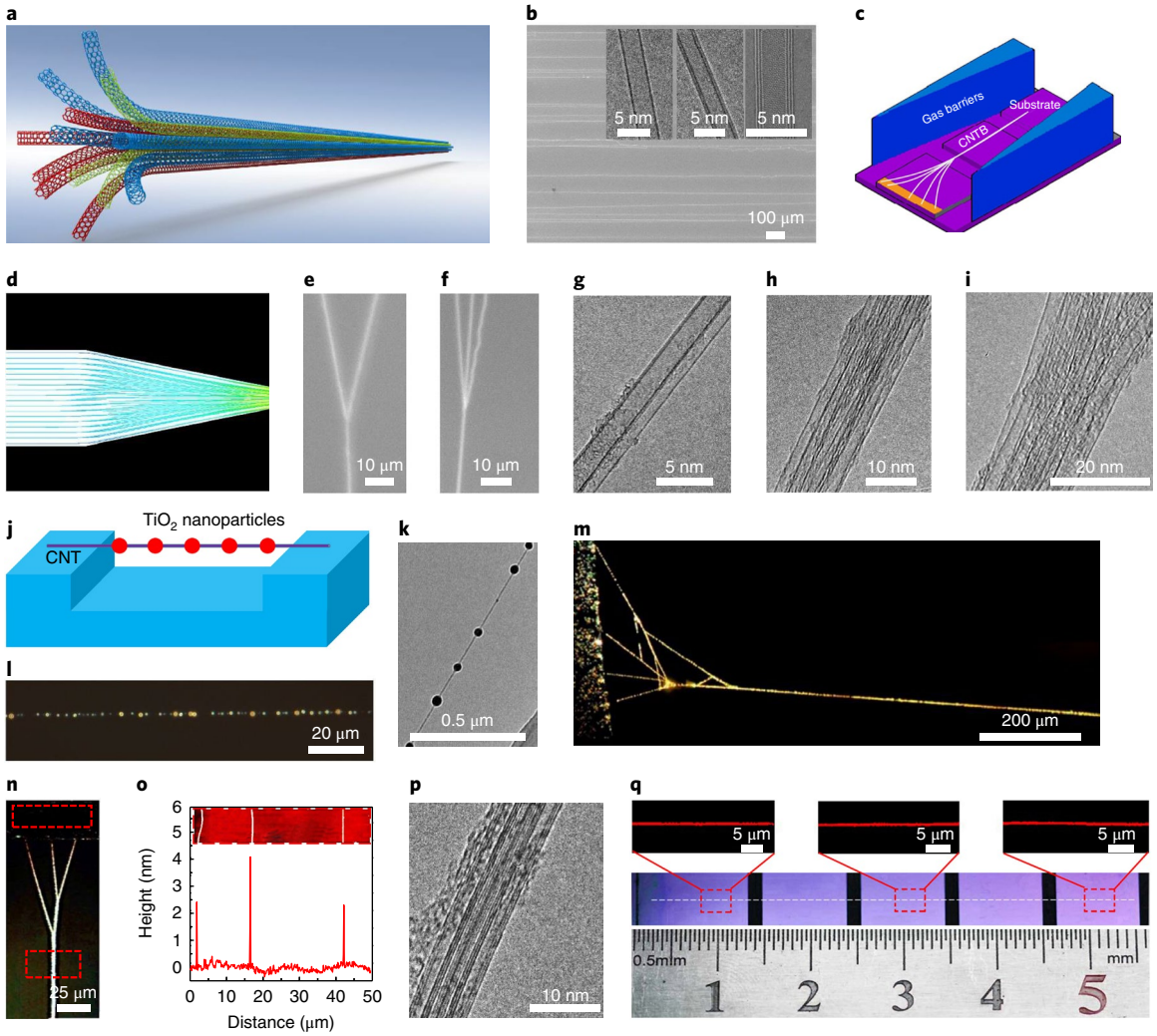

Fig. 1 | Fabrication and structural characterization of ultralong CNTBs. a, Schematic illustration of ultralong CNTBs composed of continuous CNTs. **b**, SEM image of horizontally aligned ultralong CNT arrays. Inset: high-resolution TEM images of the as-grown ultralong CNTs with single, double and triple walls. **c**, Schematic illustration of the in situ fabrication of CNTBs by the GFF method. **d**, Hydrodynamic simulation of streamline with the GFF. **e**,**f**, SEM images of CNTBs consisting of two and three CNTs, respectively. **g**–**i**, TEM images of CNTBs with different component numbers, CNTB-2 (**g**), CNTB-5 (**h**) and CNTB-10 (**i**). **j**, Illustration of decorating suspended CNTs or CNTBs with TiO_2 nanoparticles. The blue support represents a silicon substrate with a trench that allows for the suspension of the CNTs or CNTBs. **k**, TEM image of a CNT decorated with many TiO_2 nanoparticles. **l**,**m**, Optical microscopy images of a suspended CNT (**l**) and CNTB (**m**) decorated with TiO_2 nanoparticles. **n**, Optical microscopy image of a CNTB containing three CNTs. **o**, AFM image of the CNTs shown in the upper red rectangular area in **i**. **p**, High-resolution TEM image of the CNTB shown in the lower red rectangular area in **i**, showing that there are three CNTs in the CNTB. **q**, Resonance Rayleigh scattering visualization and optical image of 5-cm-long CNTs grown on an Si/SiO_2 substrate with several slits.

Unlike the previously reported micrometres-long Y-shaped CNTBs typically consisting of no more than four CNTs[24], the CNTBs that we have fabricated using the GFF method are several centimetres long and consist of 2–15 components (denoted CNTB-*n* in this paper, such as CNTB-2 and CNTB-3) (Supplementary Fig. 3). Resonance Rayleigh scattering of CNTs offers an efficient way to identify their chiral consistency (Supplementary Fig. 4)[25,26]. For the 5-cm-long CNT shown in Fig. 1q, the pure and consistent colour is identical in the resonance Rayleigh scattering images taken from three positions on the same CNT, implying a consistent chirality and defect-free structure. To measure the tensile strength of CNTBs, we use a precise micro/nanoscale material testing system (m/n-MTS) equipped with a nano-force sensing probe (Supplementary Fig. 5)[27].

Mechanical strength and Raman spectra of CNTBs

The measured tensile stress–strain curves for different CNTs/CNTBs are shown in Fig. 2a. For a single CNT, breaking occurs when the tensile stress and strain reach 121.6 GPa and 14.1%, respectively, implying the perfect structures and the superior mechanical properties of as-grown ultralong CNTs. However, for CNTBs, the mechanical properties show a remarkable decrease. Figure 2a shows the apparent stress–strain curves for three CNTBs: CNTB-2, CNTB-3 and CNTB-7. It is evident that the larger the component number, the lower the CNTBs' maximum tensile stress. The critical breaking strains of the CNTBs are also much smaller than those of single CNTs. Figure 2b shows that the apparent tensile strengths (that is, the critical tensile stress) of these CNTBs exhibit a quasi-exponential decrease with increasing *n*. In addition, the stress–strain curves shown in Fig. 2a indicate that the CNTB components exhibit a multi-stage, one-by-one breaking process under tensile loading, implying that their components have different tensile strains and thus cannot bear the loading synchronously and uniformly (Supplementary Text 3). It is noticeable that when the apparent strain is zero, the corresponding stress is not zero

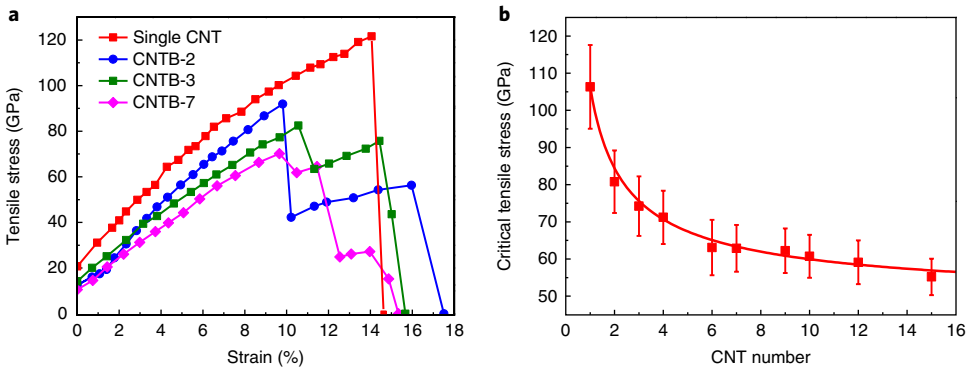

Fig. 2 | Mechanical properties of ultralong CNTs/CNTBs without any treatment. a, Stress–strain curves for single CNTs and CNTBs with gauge lengths of about 1.5 mm. **b**, The relationship between the tensile strength of CNTBs and the CNTB component numbers. The error bars denote the range of measured values, while the red squares are the mean values for each set of data.

(Fig. 2a), indicating that the suspended CNTs/CNTBs exhibit an initial strain/stress, probably introduced by the non-uniform van der Waals interaction between the suspended CNTs/CNTBs and the substrate (Supplementary Text 4).

Raman spectroscopy is used to investigate the initial strain distribution of the CNTB components. Generally, for the Raman spectra of single CNTs, there are two frequency components in the G-band: the upper frequency component (ω_G^+, associated with vibrations along the direction of the CNT axis) and the lower frequency component (ω_G^-, associated with vibrations along the circumferential direction)[28]. Both ω_G^+ and ω_G^- will have a downshift to lower frequency when there is a tensile axial strain in a suspended CNT[28–30]. As shown in Fig. 3a,b, with the increase of tensile strain in a CNTB-2, both the ω_G^+ and the ω_G^- have an obvious and continuous downshift with a rate of −8.8 and −7.8 cm^{-1} per percentage strain (% strain), respectively, which is consistent with previous reports[30,31] of G-band downshift rate ranging from −6.2 to −23.6 cm^{-1} per % strain. In addition, when a suspended CNT with initial strain is broken, both the ω_G^+ and the ω_G^- have an obvious upshift to higher frequency due to the release of the tensile strains (Fig. 3c). In Fig. 3d, the wide G-band frequency distribution for the four components in a suspended CNTB-4 clearly shows that they have different initial strains, which is the principal reason for the remarkable decrease in the tensile strength of CNTBs compared with that of single CNTs.

To discuss the relationship between the initial strain distribution and the tensile strength of CNTBs, we use a more general model of CNTBs consisting of components with different lengths and alignments. As shown in Fig. 4a (1), for a free-standing CNTB-5 consisting of five single CNTs with different lengths and alignments, if we stretch the bundle continuously until its length is just equal to the free length of the longest CNT (no CNT is broken), we can define this as the initial state of the bundle (Fig. 4a (2)). It is evident that, in the initial state, the components in this CNTB-5 have different tensile strains (defined as the initial strain). In Fig. 4a (2), the initial strain for the longest component, $\varepsilon_1 = 0$, is shown in black, and the strain for the other four components, $\varepsilon_i > 0$ ($i = 2, 3, 4, 5$), is shown in various colours. If we consider the inherent tensile strength of perfect CNTs as a constant, then the components in the CNTB have different apparent tensile strength (remnant or r-strength, defined as σ_r, $\sigma_r = \sigma_0 - \sigma_i$, where σ_0 is the inherent tensile strength of a CNT and σ_i is the initial stress) owing to the existence of the initial strain/stress. Therefore, even though the inherent tensile strength of the single CNTs remains constant, they have different apparent tensile strength when bundled together. As shown in Fig. 4a (3) and (4), the components of the CNTB-5 will break one by one when stretched together because they cannot bear the load synchronously and equally. The wide distribution of initial strain/stress of single CNTs seriously impairs the overall tensile strength of CNTBs. To improve this, the initial strains of the CNTB components should be distributed across a narrow range. As shown in Fig. 4b, for uniform alignment of CNTB components with similar strains, the tensile load can be uniformly shared across all CNTB components.

STR strategy for improving tensile strength of CNTBs

We propose a synchronous tightening and relaxing (STR) strategy to controllably release the non-uniform initial strains in the CNTB components (Fig. 4c,d and Supplementary Fig. 7). By carefully tightening and relaxing a CNTB several times, the initial strains can be released by the shrinking and slipping of components to reach almost the same value in each component. The relatively weak van der Waals interactions between CNTs play a key role in the process. The components in a CNTB remain assembled during the stretching and relaxing process, but the non-uniform initial strains cause the components to slide with respect to each other, as the axial self-driven shrinking force is larger than the van der Waals interaction between TiO_2 nanoparticles and CNTs, and between adjacent CNTs (Supplementary Text 5). The TiO_2 nanoparticles also play a unique role of maintaining the intertube connection and enhancing the tensile load transfer inside the CNTBs (Fig. 4e and Supplementary Text 6). The effect of CNT chirality on the tensile strength of CNTBs is also discussed in Supplementary Text 7.

As a consequence, after several cycles of STR, a more uniform alignment of CNTB components with similar strains is obtained (Fig. 4b). The overall G-band of a suspended CNTB-3 shifts to higher frequency after the STR treatment (Fig. 4f), clearly showing the release of the initial strains in the CNTB components. The distribution of the G-bands for the three components of the CNTB-3 becomes narrower after the STR treatment, indicating the more uniform distribution of the tensile strains in these CNTs. In addition, the G-band of a CNTB-2 measured at six different positions is the same (Fig. 4g), indicating that the CNTB (which is several centimetres long) has a consistent and continuous structure along its axial direction. More importantly, the STR treatment greatly improves the mechanical performance of the CNTBs. As shown in Fig. 4h, both the breaking strain and the tensile strength of CNTB-2, CNTB-3 and CNTB-7 are clearly improved. These results confirm that STR is an effective way to improve the uniformity of the initial strains of CNTB components.

Weibull distribution and Daniels effect

We propose a mathematical model to describe the relationship between the tensile strength of CNTBs and their component numbers and initial strains. We find that the strength, E, of single CNTs obeys the Weibull distribution, which is commonly used to describe

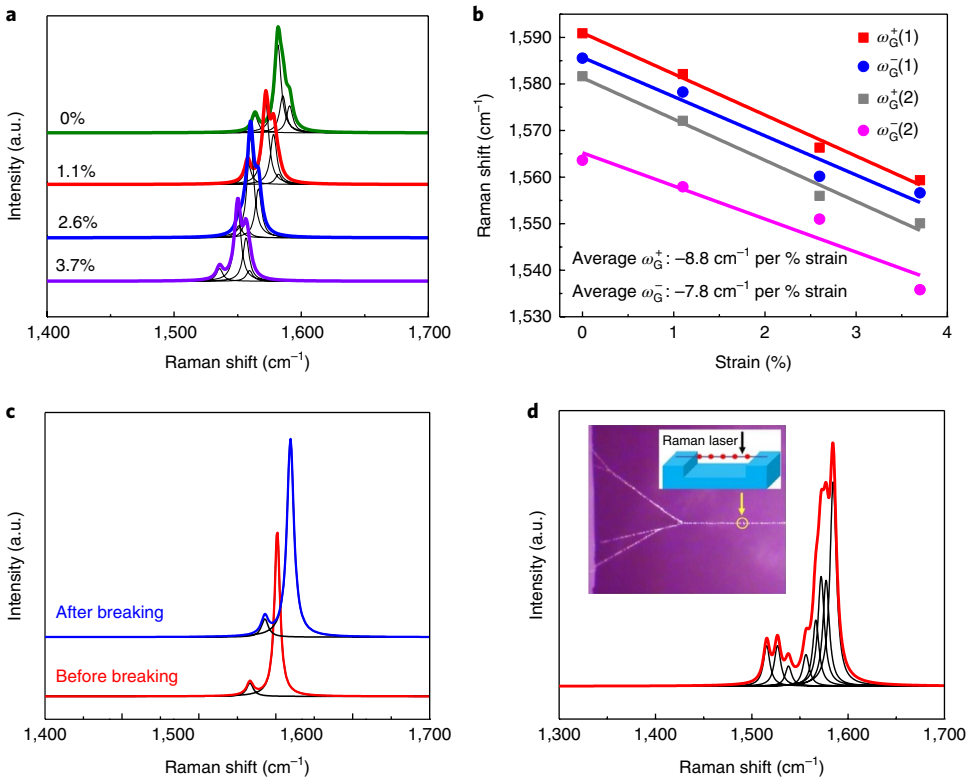

Fig. 3 | Raman spectra of as-synthesized ultralong CNTs/CNTBs. a, Raman G-band shift of a suspended CNTB-2 at strains of 0, 1.1%, 2.6% and 3.7%. **b**, G-band frequencies plotted as a function of applied strain. **c**, G-band comparison of a suspended CNT before and after breaking. **d**, G-band of a CNTB-4 shown in the inset. Inset: illustration of the Raman laser focused on the suspended CNTB-4. The broad multi-peak G-band indicates the non-uniformity of the initial strains of the components in the CNTB-4.

the strength distribution of single filaments and carbon fibres (Supplementary Text 8)[32–36]. Briefly, for single CNTs of unit length, the two-parameter Weibull distribution can be written as:

$$\ln(-\ln[1-F(\sigma)]) = \beta\ln\sigma - \beta\ln\eta \quad (1)$$

where $F(\sigma)$ is the breaking probability of single CNTs under a stress $\leq\sigma$, and η and β are the scale parameter and shape parameter of the Weibull distribution, respectively[32–34]. The mean value is written as:

$$E(\sigma) = \eta\Gamma(1+1/\beta) \quad (2)$$

and variance is written as:

$$D(\sigma) = \eta^2[\Gamma(1+2/\beta) - \Gamma^2(1+1/\beta)] \quad (3)$$

As shown in Fig. 5a, the well-fitting straight line confirms that the strength of single CNTs obeys the Weibull distribution (Supplementary Text 8).

The strength distribution of single CNTs in CNTBs can be described by a coefficient of variation (CV, also called coefficient of dispersion), which is the ratio of the standard deviation to the mean value of single CNT strength,

$$\mathrm{CV} = \sqrt{D(\sigma)}/E(\sigma) = \sqrt{\Gamma(1+2/\beta)/\Gamma^2(1+1/\beta) - 1} \quad (4)$$

A large CV value implies a highly dispersive distribution of the CNT strength. In Fig. 5a, $\beta_1 = 2.3$, $\eta_1 = 104.7$ and $\mathrm{CV}_1 = 46.1\%$ are obtained for the strength distribution of CNTs in the as-synthesized CNTBs without STR treatment. The high CV value is mainly caused by the wide distribution of initial strains of the CNTB components. In contrast, after the STR treatment, the improved values of $\beta_2 = 10.1$, $\eta_2 = 111.5$ and $\mathrm{CV}_2 = 12.1\%$ are obtained for the strength distribution of CNTs with uniform initial strains of the CNTB components. Evidently, the CV value of single CNTs decreases after the STR treatment, indicating that the strength distribution for single CNTs becomes narrower.

Daniels et al. proved that for bundles consisting of a large number (n) of single filaments with strength that obeys the Weibull distribution[37–40], the tensile strength of the bundles obeys a normal distribution with the mean value expressed as:

$$E_\sigma(n) = \sigma_0[1-F(\sigma_0)] + c_n/n \quad (5)$$

where the definition of $F(\sigma_0)$ is the same as that defined in the Weibull distribution: that is, the breaking probability of single CNTs under a stress $\leq\sigma_0$. The parameter c_n is obtained from

$$c_n = 0.966an^{1/3} \quad (6)$$

where a is a parameter that can be deduced from the boundary condition $n = 1$. The parameter σ_0 (defined as critical strength here) is the solution of $\max(\sigma[1-F(\sigma)])$. From equation (5), it is clear that the mean tensile strengths ($E_\sigma(n)$) of bundles decrease with increasing n.

The experimentally measured and theoretically calculated tensile strength of CNTBs before and after STR treatment are shown in Fig. 5b. It is evident that with increasing n there is a quasi-exponential decrease of the mean tensile strength of the CNTBs. The decrease rate of the strength decays with the increase in n,

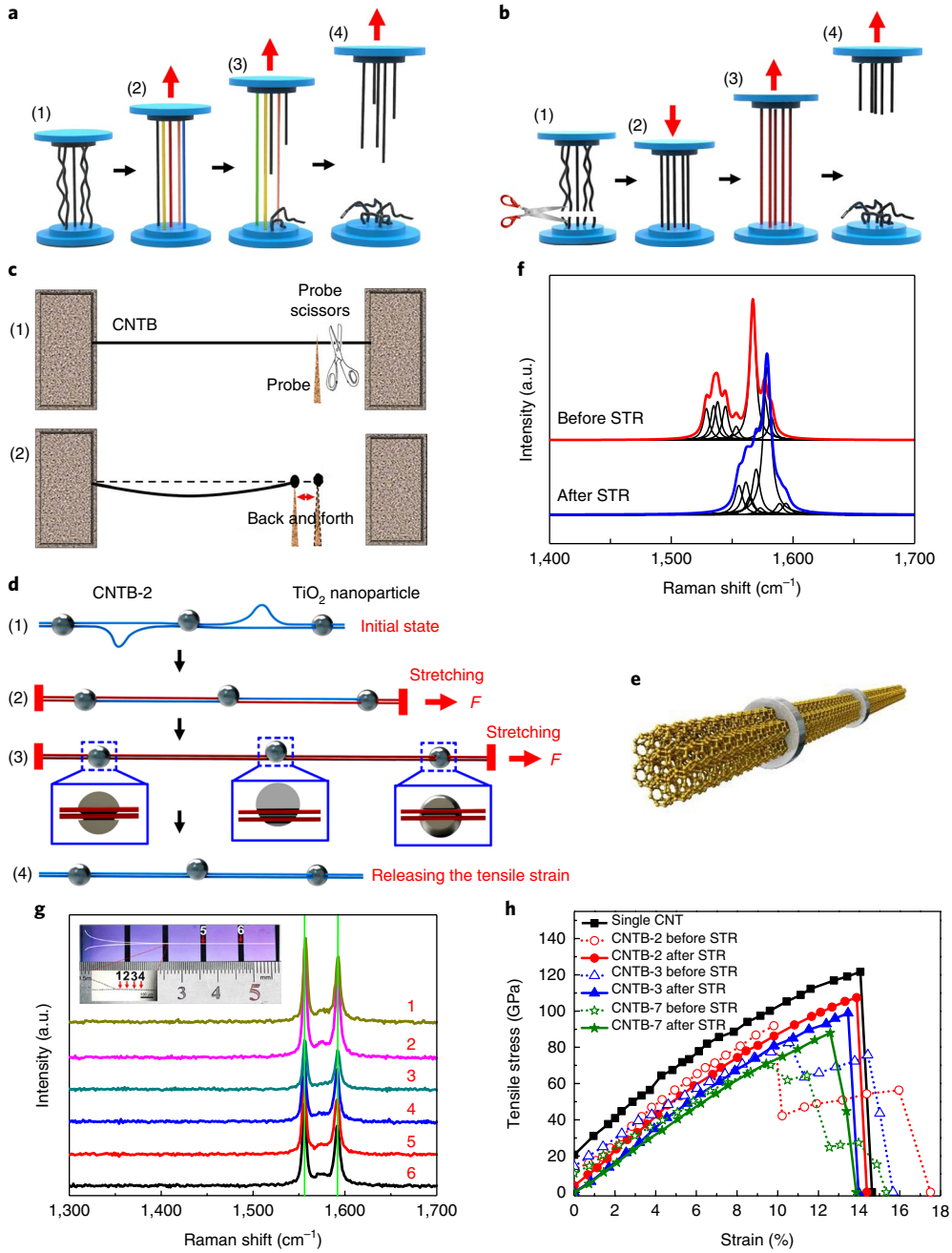

Fig. 4 | Synchronous tightening and relaxing treatment of CNTBs. a, A general model illustrating the stretching and breaking process for a CNTB with non-uniform initial strains. Different colours of CNTs in (2) mean that they have different initial strains. The change in colours between (2) and (3) indicates that the strains change. **b**, Illustration of the stretching and breaking process for a CNTB with uniform initial strains after the STR treatment. (1) Depicts cutting one end of a CNTB containing CNTs with different initial strains, (2) depicts holding the free end of a CNTB after the STR treatment and (3) depicts stretching a CNTB containing CNTs with similar initial strains. Similar colours of CNTs in (2) and (3) mean that they have similar initial strains. **c**, Illustration of the process for the STR treatment of a CNTB. **d**, Illustration of the sliding of TiO_2 nanoparticles along a CNTB-2. (1) A freely suspended CNTB-2 consisting of two single CNTs with different initial strains. (2) The CNTB-2 is stretched by tensile force *F*. The different colours indicate that the two CNTs have different tensile strains in different sections. (3) Under a larger tensile strain, the TiO_2 nanoparticles begin to slide along the CNTB-2. (4) After release of the tensile strain, the two CNTs exhibit similar initial strains with TiO_2 nanoparticles freely sliding along them. **e**, A schematic illustration showing that the TiO_2 nanoparticles work as a sheath to enhance the intertube connection inside a CNTB. **f**, G-band of a CNTB-3 before and after the STR treatment. The G-band frequency upshift indicates the release of the initial strains. **g**, G-band of a CNTB-2 at six different positions along the axial direction. Unchanged G-bands suggest the consistent and continuous structure of the centimetres-long CNTB along the axial direction. **h**, Stress–strain curves for a single CNT and for CNTB-2, CNTB-3 and CNTB-7 before and after the STR treatment.

and finally the mean tensile strength of the bundles reaches a constant value for n larger than a certain number. Figure 5b confirms that the STR treatment of the as-synthesized CNTBs can indeed improve the tensile strength of CNTBs as well as the breaking strain and toughness of CNTBs. For as-synthesized CNTBs without any treatment, when n is large enough, the mean tensile strength of the CNTBs can be as low as about 47 GPa. In contrast, after the STR treatment, the mean tensile strength of

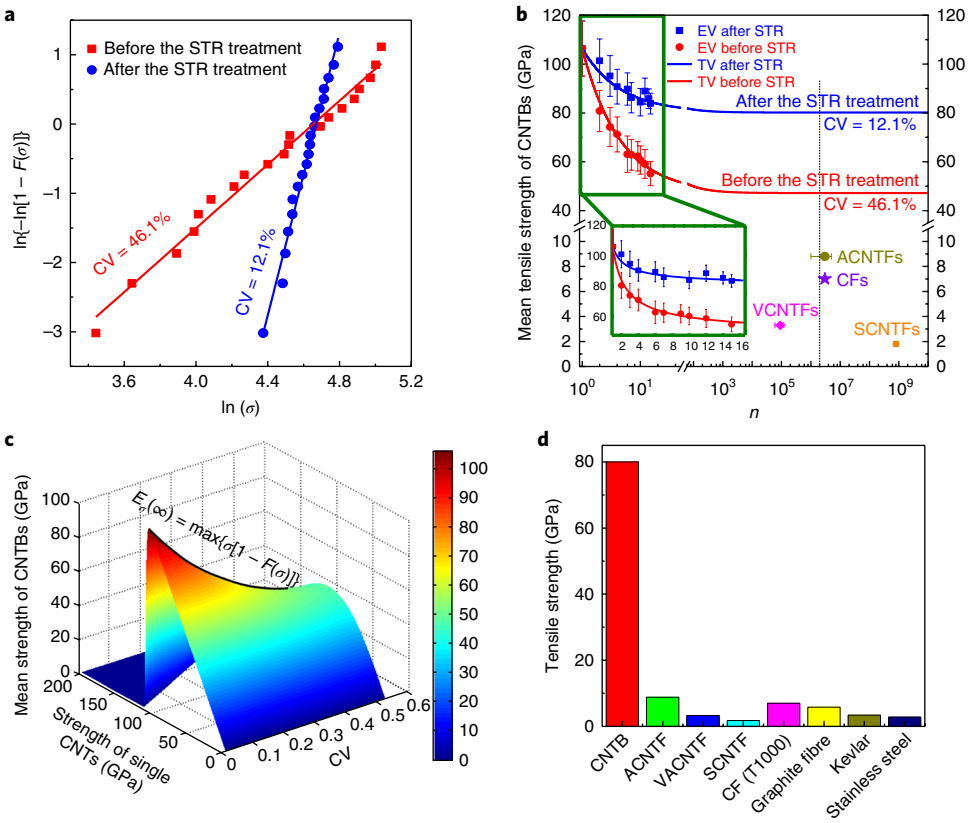

Fig. 5 | The strength of ultralong CNTBs. a, The fitting lines of $\ln\{-\ln[1-F(\sigma)]\}=\beta\ln\sigma-\beta\ln\eta$ before and after the STR treatment. From the slope and intercept of the fitted lines, we can obtain the values of β and η. **b**, The relationship between the mean tensile strength of CNTBs and their component number before and after STR treatment. The dots and curves represent the experimental value (EV) and the theoretical calculated value (TV) based on $E_\sigma(n)=\sigma_0[1-F(\sigma_0)]+c_n/n$, respectively. Statistic symbols at the bottom are the reported values for ACNTFs, CFs (carbon fibres), VCNTFs and SCNTFs. The error bars denote the range of values from multiple measurements. **c**, The relationship between the mean tensile strength of CNTBs with numerous components ($E_\sigma(\infty)$) and the strength of single CNTs (σ) as well as the coefficient of variation. **d**, Strength comparison between CNTBs, high-performance commercial materials[41,42] and other CNT fibres made by different methods, such as spinning from aerogels (ACNTFs)[14], spinning from vertically aligned CNT arrays (VACNTFs)[43] and spinning from CNT solutions (SCNTFs).

CNTBs with large n is as high as 80 GPa (the calculated specific strength of CNTBs is as high as 50 GPa cm^3 g^{-1} if taking the mean density of CNTs to be 1.6 g cm^{-3}). The strength normalized to the nanotube cross-section just before breaking would be even higher because of a positive Poisson's ratio. These results indicate that the increase of component number will not greatly affect the bundle strength provided the components are long, defect-free and with uniform initial strains. A relationship between the mean tensile strength of CNTBs with numerous components ($E_\sigma(\infty)$) and the coefficient of variation (CV) is shown in Fig. 5c. The mean tensile strength of CNTBs shows a sharp decrease with increasing CV, demonstrating the importance of improving the uniformity of the component initial strains for fabricating superstrong fibres. Figure 5d shows the strength comparison between CNTBs, high-performance commercial materials[41,42] and other CNT fibres made by different methods, such as spinning from aerogels (ACNTFs)[14], spinning from vertically aligned CNT arrays (VACNTFs)[43] and spinning from CNT solutions (SCNTFs)[44]. It is evident that the tensile strength of CNTBs is at least 9–45 times that of other materials. It should be noted that the tensile strength values of CNTBs were calculated based on the cross-sectional area of the CNTBs without including the hollow parts in CNTs, which is routine practice in the CNT community[17,45–47]. To better compare the tensile strength of CNTBs with that of macroscale engineering fibres, we also calculated the tensile strength using an engineering definition: that is, taking the whole cross-sectional area including the hollow parts in CNTs in the bundles as the base for calculating the tensile strength. The engineering values are shown in the last column in Supplementary Tables 1–7 as a reference. Using the engineering definition, the obtained tensile strength of single CNTs, CNTB-7 and CNTB with numerous components is 79 GPa, 48 GPa and 43 GPa. Thus, even if we choose the engineering definition, the tensile strength of macroscale CNTBs is still 5–24 times that of any other types of engineering fibre, indicating the extraordinary advantages of ultralong CNTs in fabricating superstrong fibres.

Conclusions

The superstrong CNTBs that we have fabricated are several centimetres long, consisting of continuous, defect-free, neat and well-aligned CNTs. The GFF method of fabrication produces CNTBs with lower tensile strength than that of individual CNTs owing to the different initial strains of individual CNTs in the bundles, but our STR strategy releases the non-uniform initial strains of the components in the bundle. With this STR strategy, the tensile strength of CNTBs consisting of a large number of components with parallel alignment, defect-free structures, continuous lengths and uniform initial strains can be as high as 80 GPa (corresponding to an engineering tensile strength of 43 GPa). Our reults show that the method provides an effective way to synthesize superstrong fibres with extremely high tensile strengths.

Methods

Methods, including statements of data availability and any associated accession codes and references, are available at https://doi.org/10.1038/s41565-018-0141-z.

Received: 10 September 2017; Accepted: 9 April 2018;
Published online: 14 May 2018

References

1. Zhang, R., Zhang, Y. & Wei, F. Horizontally aligned carbon nanotube arrays: growth mechanism, controlled synthesis, characterization, properties and applications. *Chem. Soc. Rev.* **46**, 3661–3715 (2017).
2. Appell, D. Stairway to the heavens. *Phys. World* **24**, 30–34 (2011).
3. Chae, H. G. & Kumar, S. Rigid-rod polymeric fibers. *J. Appl. Polym. Sci.* **100**, 791–802 (2006).
4. MInus, M. & Kumar, S. The processing, properties, and structure of carbon fibers. *J. Miner. Met. Mater. Soc.* **57**, 52–58 (2005).
5. Peng, B. et al. Measurements of near-ultimate strength for multiwalled carbon nanotubes and irradiation-induced crosslinking improvements. *Nat. Nanotech.* **3**, 626–631 (2008).
6. Zhang, R. et al. Superstrong ultralong carbon nanotubes for mechanical energy storage. *Adv. Mater.* **23**, 3387–3391 (2011).
7. Zhao, Q. Z., Nardelli, M. B. & Bernholc, J. Ultimate strength of carbon nanotubes: a theoretical study. *Phys. Rev. B* **65**, 144105 (2002).
8. Zhang, R., Zhang, Y. & Wei, F. Controlled synthesis of ultralong carbon nanotubes with perfect structures and extraordinary properties. *Acc. Chem. Res.* **50**, 179–189 (2017).
9. Wang, Y., Wei, F., Luo, G., Yu, H. & Gu, G. The large-scale production of carbon nanotubes in a nano-agglomerate fluidized-bed reactor. *Chem. Phys. Lett.* **364**, 568–572 (2002).
10. Ren, Z. et al. Synthesis of large arrays of well-aligned carbon nanotubes on glass. *Science* **282**, 1105–1107 (1998).
11. Zhao, M.-Q. et al. Embedded high density metal nanoparticles with extraordinary thermal stability derived from guest–host mediated layered double hydroxides. *J. Am. Chem. Soc.* **132**, 14739–14741 (2010).
12. Ding, L., Yuan, D. & Liu, J. Growth of high-density parallel arrays of long single-walled carbon nanotubes on quartz substrates. *J. Am. Chem. Soc.* **130**, 5428–5429 (2008).
13. Wen, Q. et al. 100 mm long, semiconducting triple-walled carbon nanotubes. *Adv. Mater.* **22**, 1867–1871 (2010).
14. Koziol, K. et al. High-performance carbon nanotube fiber. *Science* **318**, 1892–1895 (2007).
15. Beese, A. M. et al. Key factors limiting carbon nanotube yarn strength: exploring processing–structure–property relationships. *ACS Nano* **8**, 11454–11466 (2014).
16. Ericson, L. M. et al. Macroscopic, neat, single-walled carbon nanotube fibers. *Science* **305**, 1447–1450 (2004).
17. Zhang, X. et al. Spinning and processing continuous yarns from 4-inch wafer scale super-aligned carbon nanotube arrays. *Adv. Mater.* **18**, 1505–1510 (2006).
18. Zhang, R. et al. Growth of half-meter long carbon nanotubes based on Schulz–Flory distribution. *ACS Nano* **7**, 6156–6161 (2013).
19. Liu, Y. et al. Flexible orientation control of ultralong single-walled carbon nanotubes by gas flow. *Nanotechnology* **20**, 185601 (2009).
20. Zhang, R. et al. Optical visualization of individual ultralong carbon nanotubes by chemical vapour deposition of titanium dioxide nanoparticles. *Nat. Commun.* **4**, 1727 (2013).
21. Eder, D. & Windle, A. H. Morphology control of CNT–TiO_2 hybrid materials and rutile nanotubes. *J. Mater. Chem.* **18**, 2036–2043 (2008).
22. Georgakilas, V. et al. Decorating carbon nanotubes with metal or semiconductor nanoparticles. *J. Mater. Chem.* **17**, 2679–2694 (2007).
23. Zhang, R. et al. Superlubricity in centimetres-long double-walled carbon nanotubes under ambient conditions. *Nat. Nanotech.* **8**, 912–916 (2013).
24. Zhang, D. et al. Multiple electronic Raman scatterings in a single metallic carbon nanotube. *Phys. Rev. B* **93**, 245428 (2016).
25. Wu, W. et al. True-color real-time imaging and spectroscopy of carbon nanotubes on substrates using enhanced Rayleigh scattering. *Nano Res.* **8**, 2721–2732 (2015).
26. Zhu, Z. et al. Acoustic-assisted assembly of an individual monochromatic ultralong carbon nanotube for high on-current transistors. *Sci. Adv.* **2**, e1601572 (2016).
27. Ye, X., Zhao, L., Liang, J., Li, X. & Chen, G.-Q. Study of the tensile properties of individual multicellular fibres generated by *Bacillus subtilis*. *Sci. Rep.* **7**, 46052 (2017).
28. Dresselhaus, M., Dresselhaus, G., Jorio, A., Souza Filho, A. & Saito, R. Raman spectroscopy on isolated single wall carbon nanotubes. *Carbon* **40**, 2043–2061 (2002).
29. Zhang, Y. et al. Raman spectra variation of partially suspended individual single-walled carbon nanotubes. *J. Phys. Chem. C* **111**, 1983–1987 (2007).
30. Chang, C.-C. et al. A new lower limit for the ultimate breaking strain of carbon nanotubes. *ACS Nano* **4**, 5095–5100 (2010).
31. Chang, C.-C. et al. Strain-induced D band observed in carbon nanotubes. *Nano Res.* **5**, 854–862 (2012).
32. Nakagawa, T. & Osaki, S. The discrete Weibull distribution. *IEEE Trans. Rel.* **24**, 300–301 (1975).
33. Cohen, A. C. Maximum likelihood estimation in the Weibull distribution based on complete and on censored samples. *Technometrics* **7**, 579–588 (1965).
34. Weibull, W. A statistical distribution function of wide applicability. *J. Appl. Mech.* **18**, 293–297 (1951).
35. Chi, Z., Chou, T. W. & Shen, G. Determination of single fibre strength distribution from fibre bundle testings. *J. Mater. Sci.* **19**, 3319–3324 (1984).
36. Zhou, Y., Wang, Y., Xia, Y. & Jeelani, S. Tensile behavior of carbon fiber bundles at different strain rates. *Mater. Lett.* **64**, 246–248 (2010).
37. Daniels, H. E. The statistical theory of the strength of bundles of threads. *Proc. R. Soc. Lond. A* **183**, 405–435 (1945).
38. Lan, C., Li, H. & Ju, Y. Bearing capacity assessment for parallel wire cables. *China Civ. Eng. J.* **46**, 31–38 (2013).
39. Daniels, H. The maximum size of a closed epidemic. *Adv. Appl. Prob.* **6**, 607–621 (1974).
40. Gollwitzer, S. & Rackwitz, R. On the reliability of Daniels systems. *Struct. Saf.* **7**, 229–243 (1990).
41. MInus, M. & Kumar, S. The processing, properties, and structure of carbon fibers. *JOM* **57**, 52–58 (2005).
42. Chae, H. G. & Kumar, S. Rigid-rod polymeric fibers. *J. Appl. Polym. Sci.* **100**, 791–802 (2006).
43. Zhang, X. et al. Ultrastrong, stiff, and lightweight carbon-nanotube fibers. *Adv. Mater.* **19**, 4198–4201 (2007).
44. Dalton, A. B. et al. Super-tough carbon-nanotube fibres. *Nature* **423**, 703–703 (2003).
45. Yu, M.-F. et al. Strength and breaking mechanism of multiwalled carbon nanotubes under tensile load. *Science* **287**, 637–640 (2000).
46. Yu, M. F., Files, B. S., Arepalli, S. & Ruoff, R. S. Tensile loading of ropes of single wall carbon nanotubes and their mechanical properties. *Phys. Rev. Lett.* **84**, 5552–5555 (2000).
47. Filleter, T., Bernal, R., Li, S. & Espinosa, H. Ultrahigh strength and stiffness in cross-linked hierarchical carbon nanotube bundles. *Adv. Mater.* **23**, 2855–2860 (2011).

Acknowledgements

This study was supported by the National Natural Science Foundation of China (grant no. 21636005), the Foundation for the National Basic Research Program of China (grant no. 2016YFA0200102), the NSFC (grant nos. 11227202, 1147215) and the National Basic Research Program of China (grant no. 2013CB934203). We thank R. H. Baughman for his advice on the manuscript. We also thank P. Shi, H. Wang and H. Xie for discussions.

Author contributions

F.W., Y.B. and R.Z. conceived the project. Y.B. designed and performed the experiments, analysed the data and wrote the manuscript. R.Z. participated in the data analysis and figure design, and co-wrote the manuscript. X.Y. participated in the mechanical measurement. X.L. supervised the mechanical measurement and participated in the data analysis and manuscript preparation. Z.Z., H.X. and B.S. participated in the synthesis and characterization of ultralong CNTs/CNTBs. D.C. participated in the establishment of the mathematical model. B.L. participated in the figure processing. C.Z. and Z.J. provided theoretical assistance with hydromechanics. S.Z. participated in the manuscript preparation.

Competing interests

The authors declare no competing interests.

Additional information

Supplementary information is available for this paper at https://doi.org/10.1038/s41565-018-0141-z.

Reprints and permissions information is available at www.nature.com/reprints.

Correspondence and requests for materials should be addressed to R.Z. or X.L. or F.W.

Publisher's note: Springer Nature remains neutral with regard to jurisdictional claims in published maps and institutional affiliations.

Methods

Synthesis of suspended CNTBs. A solution of $FeCl_3$ in ethanol (0.03 M), which was used as the catalyst precursor, was deposited on a silicon substrate by micro-printing. As shown in Fig. 1c, two quartz triangular prisms were placed on a silicon substrate as gas barriers to focus the parallel gas flow. Supplementary Fig. 1 shows that the alignment of the as-grown CNTs is consistent with the streamline pattern from hydrodynamics simulation shown in Fig. 1d. To aid the manipulation of single CNTs or CNTBs, some slits (width 0.5–3 mm; depth 0.2–0.5 mm) were also fabricated on the substrate, and thus parts of the CNTs or CNTBs were suspended on the slits (Fig. 1c,j). A large quartz boat that held the substrate and barriers was put into a horizontal quartz tube with a diameter of 31 mm, which was placed in a tube furnace. After reduction in Ar and H_2 (H_2:Ar = 2:1 by volume, with a total flow of 300 standard cubic centimetres per minute, sccm) at 900 °C for 25 min, the iron precursor changed to iron nanoparticles as catalysts for the synthesis of CNTs at 1,005 °C. CH_4 and H_2 (CH_4:H_2 = 1:2 by volume, with a total flow of 75 sccm) were used as the carbon source, together with 0.43% H_2O for accelerating CNT growth. The growth time for the CNTs was about 30 min.

Micro/nanoscale material testing system for the measurement of mechanical properties. A precise micro/nanoscale material testing system (m/n-MTS) was built to measure the mechanical properties of CNTs/CNTBs, as has been used previously[27]. As shown in Supplementary Fig. 5a–c, this m/n-MTS has a two-level design to realize both coarse and fine displacement loading. It has two sets of three-axis (*XYZ*-axis) coarse translation stages and two sets of three-axis (*XYZ*-axis) fine translation stages, allowing movement from millimetres to nanometres. The left sample stage shown in the inset of Supplementary Fig. 5a indicates the coarse translation stages using piezoelectric motors with a travel distance of 12 mm and a displacement resolution of 0.2 μm, while the right sample stage indicates the fine translation stages using piezoelectric stacks with a travel distance of 6 μm and a displacement resolution of 0.5 nm. Two types of exchangeable force sensor were assembled to realize the two-level force measurement. For the coarse level, a strain-gauge force sensor was made with a force range of 200 mN and a resolution of 0.1 mN. The average stiffness coefficient is 1.25 mN μm^{-1} and the linearity and repeatability is 0.1% of the full scale. For the fine level, we used a commercially capacitive micro-force sensing probe (FT-S100, FemtoTools, Switzerland) with a force range of 100 μN and a resolution of 5 nN. Besides these two micro-force sensors, calibrated cantilever-type force sensors were also used in the practical measurements to adapt to the tested samples. This platform can be performed under both optical microscope (HIScope KH-3000, Hirox, Tokyo, Japan) (Supplementary Fig. 5d) and SEM (Quanta 450 FEG, FEI, USA) (Supplementary Fig. 5e). The HIScope optical microscope contains a microscope system with co-axial 10× zoom lens (CX-Mount CX-10C) and infinity 2 (2c) digital colour camera including an OL-350 objective for 350–3,500× magnification. This highly scalable zoom lens was based on same-axis epi-illumination and used six replaceable objective lenses, covering magnification ranges from 35× up to 7,000×. The unique optical design allowed the use of side-lighting adaptors (rotary angle lighting, directional lighting adaptor or polarizer) for the finest detailed observations. The CX-Mount lens is a lens series compatible with the standard C-mount cameras.

Calibration of force sensor and principle of mechanical measurement. Before the mechanical measurement, the force sensor was calibrated using a magnetic levitation vibrator calibration system, which has been reported previously[48,49]. Using the fine adjustment function of the m/n-MTS, the tip of the force sensor probe is placed in contact with the centre of the suspended CNTs with strong interaction and the suspended CNTs is stretched like a string with a high tensile strain (Supplementary Fig. 5f). During the measurement, the suspended CNTs or CNTBs can be firmly fixed on the substrate by van der Waals clamping without slippage, owing to the strong interaction between CNTs and the SiO_2/Si substrate (Supplementary Text 5). The entire loading process is recorded using a charge-coupled device (CCD) connected to the microscope; the elongation of the CNTs is obtained through analysis of the image sequence, and the applied load is recorded synchronously using the force sensor (Supplementary Fig. 5g). During the elongation process of the CNTs/CNTBs, the forces can be directly read out from the m/n-MTS. The tensile strengths of CNTs/CNTBs are then calculated based on their cross-sectional areas and the tensile forces. The corresponding measurement principle is shown in the inset of Supplementary Fig. 5h. We can then obtain the relationship between the applied load and the displacement at the centre of the suspended CNTs as follows.

$$T = \frac{F}{2sin\theta} = \frac{FL}{4H} \tag{7}$$

where F is the applied load at the centre of the suspended CNTs, T is the tensile load along the axis of the CNTs, θ is the angle between the initial and real-time positions, x is the displacement of the centre, and L_0 and L are the initial and current lengths.

The diameters of the CNTs/CNTBs are measured by AFM and TEM. There are two ways to define the cross-sectional area (A) of the CNTBs. In the nanoscience definition, A is defined as the sum of the cross-sectional areas of the CNTs in the bundle without including the hollow parts both inside and between CNTs: $A = \pi t \Sigma d_i$, where d_i is the ith CNT diameter (because only the outer shell of a few-walled CNT contributes to its total strength under axial tensile deformation), and t is the CNT wall thickness (0.34 nm). In the engineering definition, A is defined as the total cross-sectional area of CNTBs including all the hollow parts: $A = \pi \Sigma \left(\frac{d_i}{2}\right)^2 / 0.9069$, where d_i is the diameter of the ith CNT and 0.9069 is the maximum possible packing density of cylinders (it should be noted here that when there were fewer than three CNTs in a CNTB, we did not take the 0.9069 into consideration). The tensile stress and strain of the CNTs/CNTBs are given by the following equations (8) and (9). The specific tensile strength of CNT bundles was calculated by dividing the breaking tensile stress (σ_{max}) by the density of CNTs (in this paper we took a mean value of 1.6 g cm^{-3}). The measured data are shown in Supplementary Tables 1–7, in which the two definitions of cross-sectional area and tensile stress are denoted as A_1, A_2, and σ_1, σ_2 respectively. The tensile strength data shown in Figs. 2, 3, 4 and 5 in the main text are based on the first definition, A_1 and σ_1. During the measurement of the CNTB strength, there is also a lateral interaction due to the lateral deformation induced by the probe, which causes a deviation of the measured tensile strength. However, owing to the extremely high aspect ratio (10^5–10^6) of the as-measured CNTBs, the deviation is negligible.

$$\sigma = \frac{T}{A} = \frac{FL}{4HA} \tag{8}$$

$$\varepsilon = \frac{L - L_0}{L_0} \tag{9}$$

Transfer of CNT/CNTB sections for further characterization. A transfer technology was developed by our group to controllably manipulate and transfer individual CNTs[20,50]. A probe-type micro-manipulation platform was used to transfer CNTs or CNTBs. The manipulation was conducted under a long-working-distance metallography microscope (FS-70Z). There were four probes positioned on four pedestals on the microscope framework. The probes could be moved precisely in the X, Y and Z directions by turning the knobs fixed on the pedestals. With the assistance of TiO_2 nanoparticles, both individual CNTs and CNTBs could be cut using probes, and the CNT/CNTB segments obtained could be transferred to other substrates. For a suspended individual CNT crossing a slit on a silicon substrate, two probes could be used to cut the CNTs. The probes then served as tweezers to transfer the cut-off segment. After that, the probes were moved away from the CNT segment. The segments could also be transferred to other substrates and be directly used for further characterizations, such as Raman spectra measurement, TEM characterization and electrical measurement. A silicon substrate with marks was used to precisely locate the position of the CNTs/CNTBs (Supplementary Fig. 6a). Cut-off CNT/CNTB sections could be directly transferred onto a TEM grid with marks (Supplementary Fig. 6b,c), which greatly aid the fast and precise positioning of CNT/CNTB sections for the following high-resolution TEM characterization to obtain more structural information.

Attachment, detachment and reattachment of CNTs/CNTBs with probes. We have previously found that there was a strong interaction between the suspended CNTs and metal probes[20,50]. For example, when a metal probe was approaching a suspended CNT, the CNTs would be attracted towards the probe even though they were not in contact with each other[20]. The interactions between them stem from both the van der Waals interaction and the electrostatic forces of the metal probe. Once the suspended CNT came into contact with a metal probe, it would be firmly fixed onto the probe. The attachment between CNTs and probe was large enough to stretch the CNTs until the outer shell was broken without any slippage during the whole process[20,50]. Therefore, it was easy to use just two metal probes to cut a section from a suspended CNTs or CNTBs.

In the previous section, we introduced the transfer of CNTs or CNTBs onto other substrates using probes. There are two ways to detach the samples quickly from the probes[23]: either rub the contact section of CNTs and probe on the substrate to drag the CNTs off the probe, or apply a current through the metal probe to burn the CNTs. To reattach the CNTs/CNTBs to the metal probes, one just needs to move the probe into contact with the samples to create reattachment due to the strong interaction between them.

STR treatment of CNTBs. As-synthesized suspended CNTBs on the substrate were put under an optical microscope (Supplementary Fig. 7(1)). As discussed in the Methods section above, there is a strong interaction between CNTs and metal probes, so the suspended CNTBs could be firmly fixed by two metal probes near one end of the suspended section (Supplementary Fig. 7(2)). Keeping the left probe unmoved, we moved the right probe to the right end until the right section of the suspended CNTB was broken (Supplementary Fig. 7(3) and (4)) and then moved the right probe away (Supplementary Fig. 7(5)). Then, by moving the left probe back and forth within a narrow range in the axial direction of CNTB (Supplementary Fig. 7(6)), the widely distributed initial strains could be released by

the self-driven shrinking and slipping of adjacent CNTs (see Supplementary Text 5) to produce a narrower distribution of initial strains in the bundle.

Other characterization. The CNTs/CNTBs were inspected by SEM (JSM 7401F, 1.0 kV), Raman spectrometer (Horiba HR 800, 632.8 nm) and TEM (JEM 2010, 120.0 kV). An optical microscope (long-working-distance metallography microscope, FS-70Z) and a supercontinuum laser were used for resonance Rayleigh scattering. Another optical microscope (HIScope KH-3000, Hirox, Tokyo, Japan) was used for optical characterization and manipulation of CNTs/CNTBs. Resonance Rayleigh scattering was used to identify the chiral consistency of individual CNTs. As shown in Supplementary Fig. 4, when illuminated by the wide-field supercontinuum laser, single CNTs with different chiral structures exhibit different colours.

Data availability. The data that support the plots within this paper and other findings of this study are available from the corresponding authors upon reasonable request.

References

48. Wang, W. et al. Measurement of the cleavage energy of graphite. *Nat. Commun.* **6**, 7853 (2015).
49. Li, Q., Kim, K.-S. & Rydberg, A. Lateral force calibration of an atomic force microscope with a diamagnetic levitation spring system. *Rev. Sci. Instrum.* **77**, 065105 (2006).
50. Zhang, R. et al. Facile manipulation of individual carbon nanotubes assisted by inorganic nanoparticles. *Nanoscale* **5**, 6584–6588 (2013).